ADVANCED OPTICAL MATERIALS
www.advopticalmat.de

Impact of Halogen Groups on the Properties of PEA-Based 2D Pb–Sn Halide Perovskites

*Elham Foadian, Sheryl L Sanchez, Sumner B. Harris, Benjamin J. Lawrie, Astita Dubey, Yipeng Tang, Bin Hu, Jonghee Yang, and Mahshid Ahmadi**

Tuning broad emission in 2D Pb–Sn halide perovskites (HPs) is essential for advancing optoelectronic applications, particularly for color-tunable and white-light-emitting devices. This broad emission is linked to structural factors, such as defects and phase segregation of the Pb component within the Pb–Sn system, which are strongly influenced by the molecular structure and chemical properties of spacer cations. Atomic tuning of the spacers via halogenation opens up a new way to fine-tune the molecular properties, enabling further augmentations of HP functionalities. Nevertheless, the distinct broad emission's sensitivity to spacer chemistry remains underexplored. Here, halogenation's influence is systematically investigated on 2D HP emission characteristics using a high-throughput workflow. These findings reveal that the F-containing phenethylammonium (4F-PEA) spacer narrows the broadband PL, whereas Cl broadens it. Through a correlative study, it is found that 4F-PEA reduces not only the local phase segregation but also the defect levels and microstrains in 2D HPs. This is likely attributed to the manifestation of less lattice distortion via stronger surface coordination of the dipole-augmented 4F-PEA. These results highlight halogenation as a key factor in modulating phase segregation and defect density in 2D Pb–Sn HPs, offering a promising pathway to tune the emission for enhanced optoelectronic performance.

1. Introduction

2D halide perovskites (HPs) have emerged as promising materials in the advancement of optoelectronic applications, offering a notable advantage in stability over their 3D counterparts.[1] Although 2D HPs offer significantly improved stability, they generally display a wider bandgap and weaker charge transport due to the insulating nature of organic spacer layers. This can lead to reduced device performance when compared to 3D HPs.[2] Recently, a number of studies have shown that fluorinating spacer cations—such as fluorinated bromobenzyl ammonium (F-BBA),[3] fluorinated phenylethyl ammonium (F-PEA),[4] and fluorinated aromatic formamidinium (F-ArFA)[5] can significantly improve the charge transport, power conversion efficiency and stability of HP solar cells. A study by Bala et al. indicates that using fluorinated or chlorinated organic spacer cations (F-PEA and Cl-PEA) could lead to HP solar cells that are both highly efficient and stable.[6] The proposed mechanisms include vertically aligned crystal growth for better charge transport in quasi 2D HPs,[7] promoting type-II energy-level alignment to prevent carrier trapping and recombination,[8] and reducing trap density while increasing carrier mobility.[4] The distinct electronegativities of fluorine (3.98) and chlorine (3.16) on the Pauling scale, along with the larger size of chlorine, could influence the characteristics of the resulting organic molecules.[9] However, the relationship between the fluorination of spacer cations and broadband photoluminescence (PL) emission in 2D mixed Pb–Sn HPs remains unexplored.

2D mixed Pb–Sn HPs have demonstrated remarkable effectiveness both as standalone active layers and as the top cell in tandem configurations.[10] Adjusting the Pb to Sn ratio within these materials allows for precise tuning of the band gap between 1.6 to 2.4 eV.[10] This customization not only enhances charge carrier dynamics compared to HPs containing only Pb but also offers superior stability compared to those solely based on Sn.[11] Interestingly, these materials diverge from the expected narrow-band PL, instead exhibiting broadband emission characterized by a significant Stokes shift.[12] This unique property enables them to emit photons across the entire visible spectrum, resulting in the generation of broadband white light.[13] In our recent work, we discovered that broadband PL emission in 2D

E. Foadian, S. L Sanchez, A. Dubey, Y. Tang, B. Hu, M. Ahmadi
Institute for Advanced Materials and Manufacturing
Department of Materials Science and Engineering
University of Tennessee
Knoxville, TN 37996, USA
E-mail: mahmadi3@utk.edu

S. B. Harris, B. J. Lawrie
Center for Nanophase Materials Sciences
Oak Ridge National Laboratory
Oak Ridge, TN 37831, USA

B. J. Lawrie
Materials Science and Technology Division
Oak Ridge National Laboratory
Oak Ridge, TN 37831, USA

A. Dubey
Institute for Materials Science and Center for Nanointegration
Duisburg-Essen (CENIDE)
University of Duisburg-Essen
Universitätsstr. 15, 45141 Essen, Germany

J. Yang
Department of Chemistry
Yonsei University
Seoul 03722, Republic of Korea

The ORCID identification number(s) for the author(s) of this article can be found under https://doi.org/10.1002/adom.202403120

DOI: 10.1002/adom.202403120

mixed Pb–Sn HP ($PEA_2Pb_nSn_{1-n}I_4$) arises from defect-induced Stokes shifts and charge transfer excitons formed by phase segregation. Crucially, these phenomena are closely tied to the Pb: Sn ratio, highlighting the role of composition in dictating the perovskites' optical properties. However, it can be also influenced by a multitude of other factors beyond the Pb: Sn ratio. Compositional engineering involves fine-tuning elements within the material's structure, each adjustment offering a pathway to precisely control and optimize its emission characteristics.[14]

Defect formation and phase segregation are critical challenges in 2D mixed Pb–Sn HPs that significantly affect their optoelectronic performance and stability. Common defects in these materials include vacancies (e.g., Pb, Sn, or halide vacancies), interstitials, and antisite defects, where atoms occupy incorrect lattice sites.[15] These defects can act as non-radiative recombination centers, reducing PL efficiency and carrier lifetimes. Oxidation-related defects, such as the formation of Sn^{4+} and metallic Sn, are also prevalent in Sn-containing perovskites, contributing to material degradation.[16] Phase segregation in 2D Pb–Sn HPs arises from several factors; One key reason is the intrinsic differences in the ionic sizes and bonding preferences of Pb^{2+} and Sn^{2+}, which create lattice strain and uneven chemical potential distribution, leading to the separation of Pb and Pb–Sn phases.[17] Additionally, the difference between the crystallization rates of Pb and Sn plays a significant role, as Sn exhibits a much faster crystallization rate compared to Pb, which can result in inhomogeneous distribution during film formation and exacerbate phase segregation.[18] Phase segregation typically manifests in two primary forms; spatial separation within the lattice, resulting in localized mixed Pb–Sn and Pb regions, and temporal evolution, where segregated phases grow with prolonged environmental exposure or under stress conditions such as illumination or heat. This segregation disrupts charge transport pathways and broadens the emission spectrum, undermining the stability and performance of optoelectronic devices. These challenges highlight the need for effective strategies, such as chemical engineering of spacer cations, using appropriate additives or samples processing to suppress defect formation and phase segregation, thereby improving material properties.

Building on our previous study, we aim to explore how spacer cation engineering, specifically introducing F and Cl into the PEA phenyl ring, affects broadband emission in 2D Pb–Sn HPs. Atomic tuning with F and Cl alters molecular properties—such as dipole moments and ionic sizes—which influence defect formation, phase segregation, and lattice stability within the 2D Pb–Sn system. These molecular modifications are anticipated to affect emission behavior by modulating the electronic structure and defect density, leading to changes in broad emission characteristics. To explore that, we conduct a thorough examination of how these spacer cations influence the spectral properties of mixed Pb–Sn 2D HPs, leveraging a high-throughput automated synthesis-characterization process. We synthesized 2D mixed Pb–Sn HP drop-casted films with 288 different compositions using an automated drop-casting method, completing the entire process in just three hours. Utilizing high-throughput optical characterization efficiently investigates the dynamic changes in PL spectral features, including broadband emission and phase segregation behavior over time—tasks that are beyond the speed and scope of manual experimentation. Our findings demonstrate that introducing a fluorinated cation as a spacer reduces phase separation and narrows broadband emission (reduced FWHM), resulting in fewer defects, microstrains, and less lattice distortion. This can be attributed to fluorine's higher electronegativity and dipole moment, which enhance the stability of the lattice by lowering distortion and reducing defect sites. In contrast, using a chlorinated cation accelerates phase segregation and broadens emission, leading to films of lower quality. Chlorine's larger ionic size introduces greater lattice strain and microstrain, promoting phase segregation and defect formation. The controllable modulation of phase segregation and defect density by halogenation in 2D Pb–Sn HPs offers a promising pathway to tune the PL emission for enhanced optoelectronic performance.

2. Results and Discussion

We investigate the PL emission characteristics of 2D Pb–Sn HPs and explore the evolution across 288 distinct compositions by varying the Pb: Sn ratio and three different spacer cations, using PEA, and adding halogen groups (F and Cl) into it. To facilitate this exploration, we utilize a high-throughput automated experimental workflow that includes an automated synthesis, rapid PL characterization, and automated data analysis. This automated method allows for precise control over key parameters such as mixing the precursor solution in stoichiometric ratios, pipette height for uniform deposition of solutions in the entire library, resulting in controlled film properties, including film quality and uniformity. Moreover, this method minimizes chemical consumption and waste during exploration, using just 0.5 µL of solution per sample. The comprehensive experimental workflow employed is depicted in **Figure 1**. PEA_2PbI_4 and PEA_2SnI_4 precursor solutions, prepared in 96 distinct ratios, are mixed within a well plate. Each solution is then uniformly distributed onto a heated glass substrate (at 100 °C) by a pipetting robot, forming uniform thin films (Figure 1a). To explore the effect of spacer cations, this experiment was conducted using 4F-PEA and 4Cl-PEA as spacer cations with the same method. Consequently, we utilize three separate wellplates (a total 288 films) to systematically explore the effects of these variations on PL characteristics (Figure S1, Supporting Information). After the synthesis of HP films, we monitor the temporal changes in PL behaviors of the 2D Pb–Sn HPs using a high throughput optical reader, assessing the impact of time and composition ratios on broadband emission (Figure 1a). Figure S2 (Supporting Information) shows PL spectra of the 2D Pb–Sn HP drop-casted films collected over 15 h, consisting of 9600 individual spectra for each dataset (96 compositions with 100 measurement cycles, 28 800 spectra in total for all 288 compositions). There are two peaks observed in these compositions, a peak ≈520 nm, attributed to the segregated phase of the Pb component, and a broad peak ≈670 nm, corresponding to the broadband emission of the 2D Pb–Sn HPs.[18] Then, an automated peak-fitting function was implemented to analyze the large PL dataset (Figure 1b) allowing for the evaluation of the PL properties including the full-width at half-maximum (FWHM) of broad emission and peak intensity of the segregated phase, associated with the corresponding composition, all within just 45 min. To provide a detailed examination of the impact of various parameters, including the spacer cations and the Pb: Sn ratio in $X_2Pb_nSn_{1-n}I_4$ as represented by the

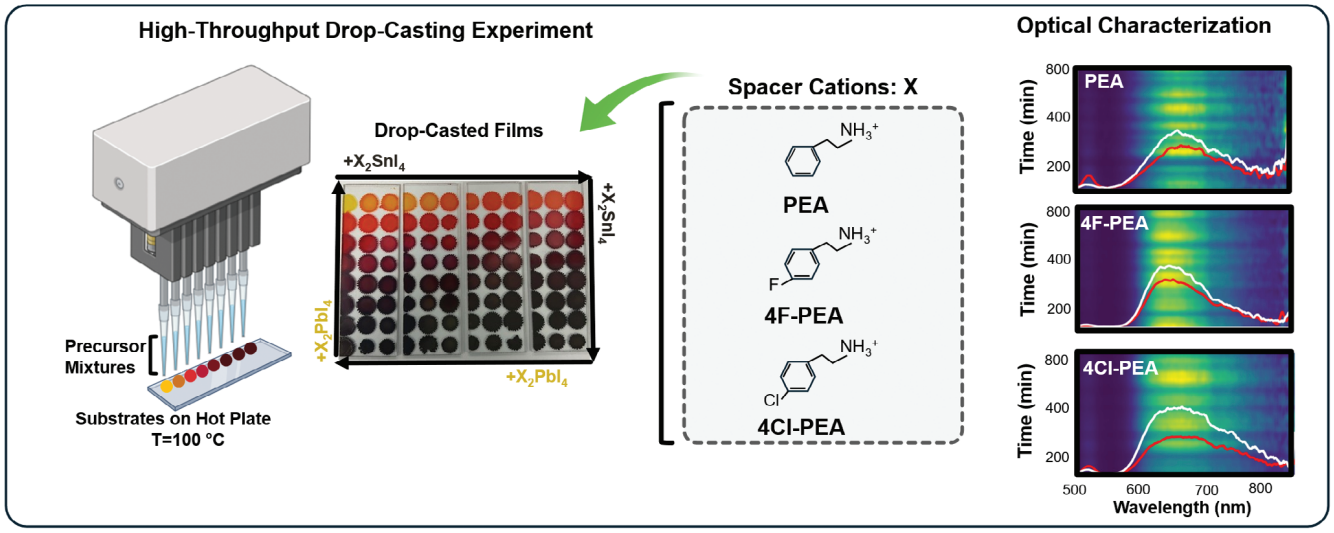

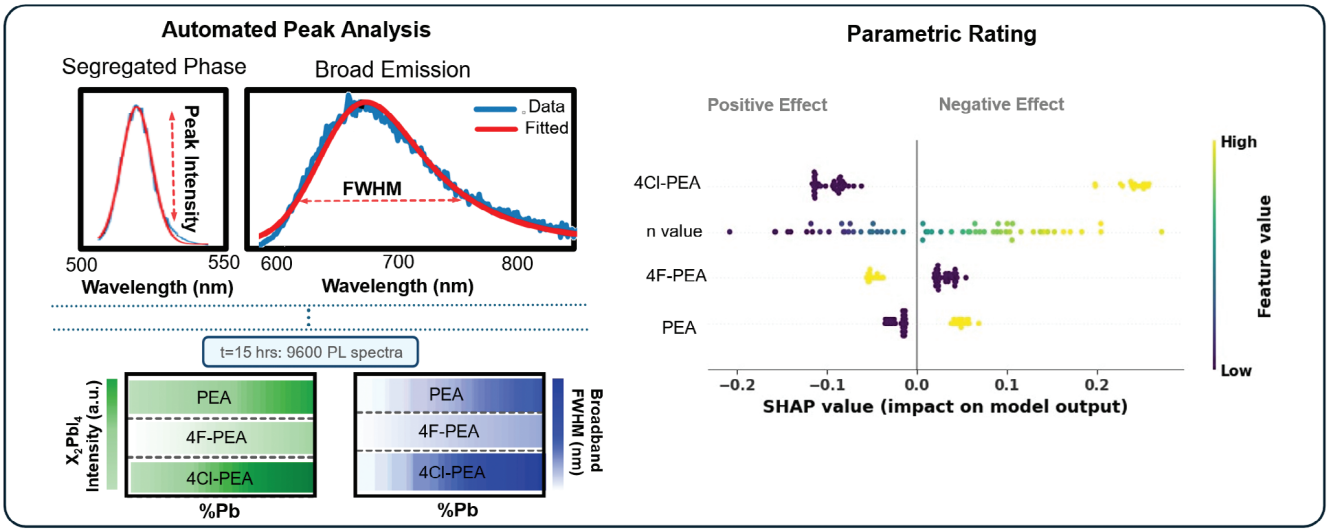

Figure 1. Automated experimental workflow of 2D Pb–Sn HPs films. a) High-throughput automated synthesis of 2D HP drop-cast films with 96 different compositions: combinatorial mixing of X_2PbI_4 and X_2SnI_4 endmember precursors by a pipetting robot, using three spacer cations (X = PEA, 4F-PEA, and 4Cl-PEA). Each precursor mixture was drop-casted on glass substrates by 8 channel pipetting robot and annealed at 100 °C, and high-throughput automated PL characterizations of the drop-casted films for 15 h, providing 9600 individual PL spectra. b) automated data analysis of 9600 PL spectra, enabling tracking of PL properties over time, along with the SHAP plot with rating the impact of each feature value on the intensity of phase segregation.

n value, on the phase segregation and broad emission, we utilized a machine learning method "Shapley Additive Explanations" (SHAP). SHAP is a powerful tool that can assign positive or negative impacts to each parameter on the overall prediction of the system.[19] Consequently, this optimized workflow facilitates a comprehensive and expedited exploration of the effects of compositional variations on PL characteristics.

To accelerate the analysis of PL behaviors, we utilize a peak-fitting function to analyze changes in the intensity of the segregated phase and the FWHM of the broad emission in the films. Here, we visualized the intensity of the segregated phase (PL peak centered at ≈525 nm) and FWHM of broad PL emission (centered at 670–700 nm), respectively in the color map of **Figure 2a–c**. The lighter colors represent the low intensity of the segregated phase and/or narrow FWHM and the darker sections, on the other hand, denote the higher intensity of the segregated phase and/or broader FWHM. It is clearly observed that using 4F-PEA results in a lower intensity of phase segregation compared to PEA and 4Cl-PEA at the initial time. Although the intensity of phase segregation in the film increases after 15 h for all compositions, as represented by the darker color in Figure 2a–c, the compositions with 4F-PEA exhibit a lower intensity of the

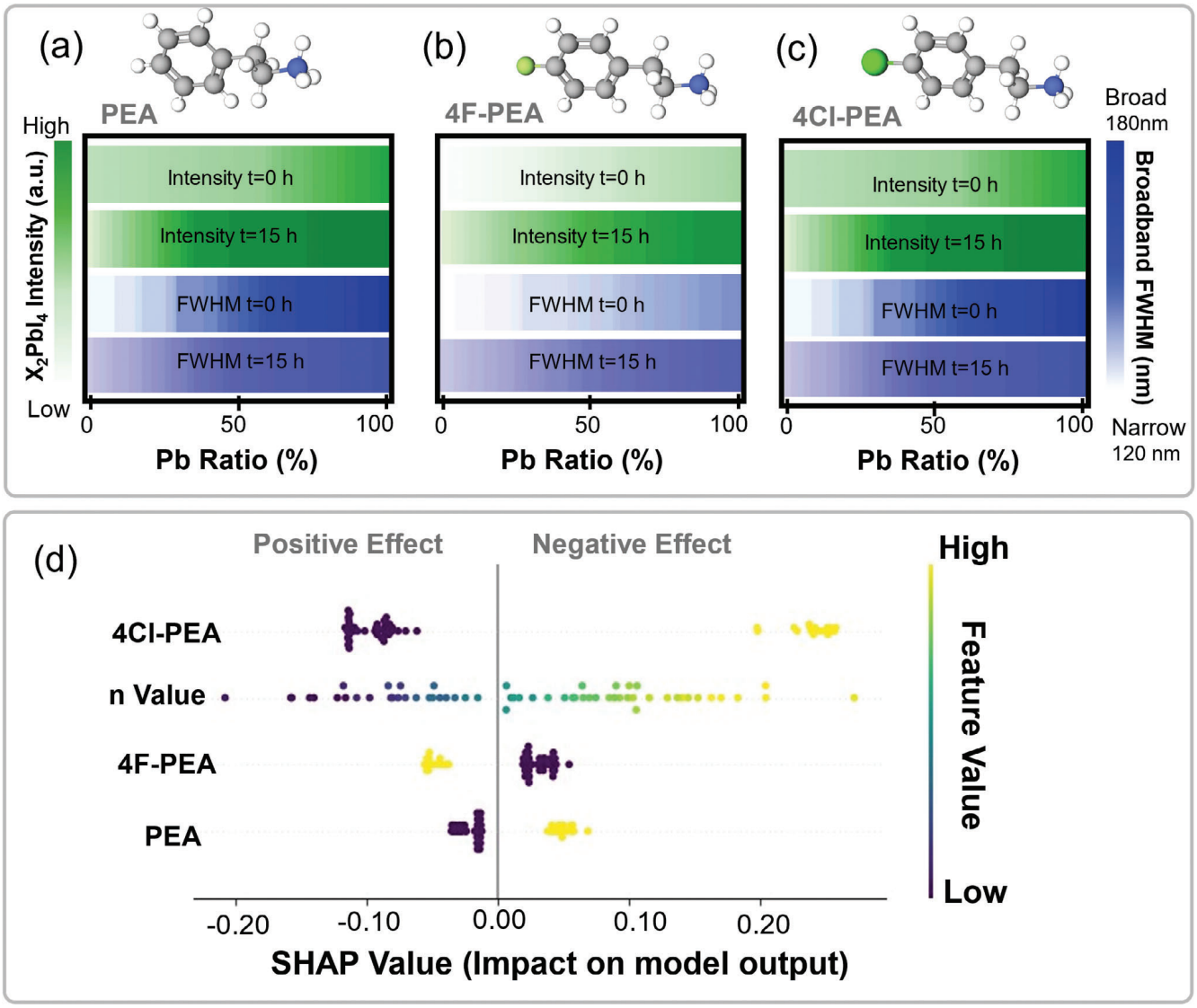

Figure 2. PL characterization of $X_2Pb_nSn_{1-n}I_4$ drop-casted films, the color map of the changes in phase segregation intensity (Green), and the color map of the changes in the FWHM of broad emission (Blue), at the initial time and after 15 h, for the 96 different Pb–Sn ratio compositions, using a) PEA, b) 4F-PEA and c) 4Cl-PEA as spacer cations. d) The ranking of feature importance using SHAP assessment, showing the impact of each composition on the intensity of phase segregation in descending order of importance (rank). The purple and yellow colors indicate low and high values of a given feature, respectively.

segregated phase after this period (Figure 2b). As demonstrated previously,[12,18,20] defects and phase segregation are regarded as two key factors associated with peak broadening mechanisms in 2D Pb–Sn HPs. The variations in the intensity of phase segregation by changing spacer cation can influence the FWHM of broad emission. Figure 2b illustrates that reducing the phase segregation in compositions with 4F-PEA results in narrower emissions at both initial and final measurements regardles of Pb: Sn ratios. While using 4Cl-PEA results in higher phase segregation intensity and increased FWHM of broad emission compared to PEA as depicted in Figure 2c. These observations clearly demonstrate that in addition to Pb: Sn ratios that affect broad emission and phase segregation in 2D Pb–Sn HP,[18] other factors such as the choice of spacer cations can influence the PL characteristics. The distinct effects of fluorinated and chlorinated spacer cations on PL characteristics can be attributed to their respective dipole moments and atomic sizes, which impact lattice strain and defect formation. It means, Fluorine's high dipole moment promotes stable bonding between spacer cations and an inorganic layer of the perovskite lattice and reduced defects,[21] while chlorine's larger ionic radius induces lattice distortion,[22] promoting phase segregation and broadened emission.

To summarize how various parameters, such as n values of the $X_2Pb_nSn_{1-n}I_4$ structure (Pb: Sn ratio) and different spacer cations (X = PEA, 4F-PEA, and 4Cl-PEA) influence the emergence of phase segregation, we utilized SHAP, a powerful machine learning (ML) method. Briefly, SHAP is an explainable ML method that applies game-theoretic principles to quantify each feature's contribution to model predictions. This approach provides ranked feature importance and reveals trends in how

each feature influences the target variable. Using SHAP in this case is especially beneficial compared to traditional statistical methods, as it enables a higher degree of interpretability, particularly for complex, non-linear relationships within the data.[23] In particular, a positive/negative SHAP value indicates that the input property with the given value (indicated by color: yellow for high values and purple for low values) positively/negatively affects the output variable (intensity of segregated phase), while the modulus indicates the weight of this influence. We trained four distinct models—linear regression, random forest regression, support vector machine, and neural network—to discern patterns in the changes of phase segregation intensity. The root-mean-square error was computed for each model to assess the average difference between the predicted values and the actual values of the peaks, as shown in Figure S3 (Supporting Information). The neural network and linear regression models proved to be the most effective. SHAP then calculates the contribution of each feature to the prediction by considering all features and their interactions.[24] The linear regression model was employed to evaluate the intensity of phase segregation. Subsequently, SHAP was used to rank the importance of each parameter. Our analysis reveals that the higher Sn content in the compositions (lower n values), along with the use of 4F-PEA, positively impacts the system, resulting in a lower intensity of phase segregation as shown in Figure 2d. Conversely, a higher Pb content in the samples (*n*-values) and the use of 4Cl-PEA and PEA as spacer cations have a negative impact, leading to an increase in the intensity of phase segregation. These observations suggest that the fluorination of spacer cation reduces phase segregation – likely associated with the enhanced dipole moment of 4F-PEA – realized by the high electronegativity of fluorine.[4,25] These properties lead to stronger interactions between the fluorinated cation and the inorganic layers, enhancing crystal stability and minimizing defects.[26] In other word, stronger spacer-inorganic interactions improve crystal stability by creating a tightly bonded structure, which reduces lattice distortions and makes defect formation less likely. This bonding reinforces the crystal lattice, minimizing weak points where defects typically develop. The result is a more stable and defect-resistant structure. The stronger coordination of spacer cation can manifest a more rigid lattice structure where the ionic movements are greatly restricted. In turn, this can effectively suppress the phase segregation and the consequent establishment of the charge transfer state, which is likely associated with the broadband emission. That is, the lower phase segregation narrows the FWHM of broadband PL. In contrast, Cl with its larger size and weaker bonding, increases phase segregation. The larger atomic radius introduces strain within the lattice,[27] while the weaker bonding with the inorganic layer, reduces the stability of the material. This promotes defects and phase separation, leading to broader emission peaks (increased FWHM) associated with higher phase segregation and degraded material performance.

Figure S4 (Supporting Information) visualizes the PL spectra for three selected Pb–Sn ratios from the high-throughput dataset, chosen to highlight representative emission trends across compositions. The initial and final PL peaks for each composition are also displayed in this figure. Predictably all the mixed Pb–Sn HPs exhibit broad emission peaked at ≈700 nm which corresponds to the 2D Pb–Sn HPs.[12,28] Figure S4a–c (Supporting Information) shows that the broadband emission becomes broader with increasing Pb composition ratios, irrespective of the spacer cations, as we observed previously.[] In addition, tiny but evident bumps of X_2PbI_4 emission at ≈520 nm are also observed in the films with 50% and 90% Pb ratios (Figure S4b,c, Supporting Information), confirming that phase segregation occurs at high Pb ratios, which is not appreciable in the film with a 10% Pb ratio (Figure S3a, Supporting Information), suggesting the slow segregation behaviors at these lower ranges. Meanwhile, while all films display a noticeable decline in broadband PL intensity over time from initial to final measurements—suggesting ambient degradation—the intensity of the segregated phase increases after 15 h, pointing to the growth of this phase (illustrated by the white and red spectra shown in Figure S4, Supporting Information). Overall, this figure confirms that using 4F-PEA spacer results in higher FWHM of broad emission and lower intensity of the phase segregation compared to the PEA and 4Cl-PEA for all selected samples.

To confirm the results from high-throughput drop-casted films are transferrable to the laboratory practice among the perovskite community, the PL behaviors of spin-coated 2D HPs thin films were investigated using standard HP thin film fabrication method for three different Pb ratios and spacers (Detailed in the experimental section) and similarly studied the PL features, FWHM of broad emission and intensity of segregated phase using peak-fitting functions and shown in Figure S5 (Supporting Information). Figure S5a (Supporting Information) illustrates the intensity of phase segregation for three selected Pb ratios (10%, 50%, and 90%) using three different spacer cations, both at the initial time and after 15 h. These Pb compositions were chosen to match those used in the drop-casted films, allowing for direct comparison. The results confirm that across all Pb: Sn compositions of the thin films, the use of 4F-PEA leads to a lower intensity of phase segregation, while 4Cl-PEA results in a higher intensity of phase segregation compared to PEA, consistent with the high-throughput findings. Figure S5b (Supporting Information) further demonstrates the impact of spacer cations on the FWHM of the broadband emission in these compositions, showing that 4F-PEA reduces the FWHM, whereas 4Cl-PEA broadens the emission peak. These findings validate the high throughput synthesis results, regardless of the deposition technique used.

To gain spatially resolved insights into the effects of fluorination of PEA spacer cation on the phase segregation reduction and its impact on the emission of 2D Pb–Sn HP films, hyperspectral cathodoluminescence (CL) microscopy is employed,[29] to analyze several selected Pb–Sn films with using PEA and 4F-PEA as spacer cations. **Figure 3** displays the CL results for samples with a 90% Pb ratio. We selected the samples with high Pb content from different Pb–Sn compositions, as phase segregation is more pronounced in them, allowing for a thorough comparison. The corresponding SEM images in Figure 3a reveal nominal surface morphologies characterized by flattened surfaces. Maps filtered at 520 nm in Figure 3b, which highlight the segregated phase, distinctly reveal clear local contrasts on these film surfaces. Additionally, it is observed that the use of 4F-PEA significantly reduces phase segregation in the CL maps compared to PEA similar to our PL studies. These contrasts are aligned with the SEM images, which show both segregated phases and

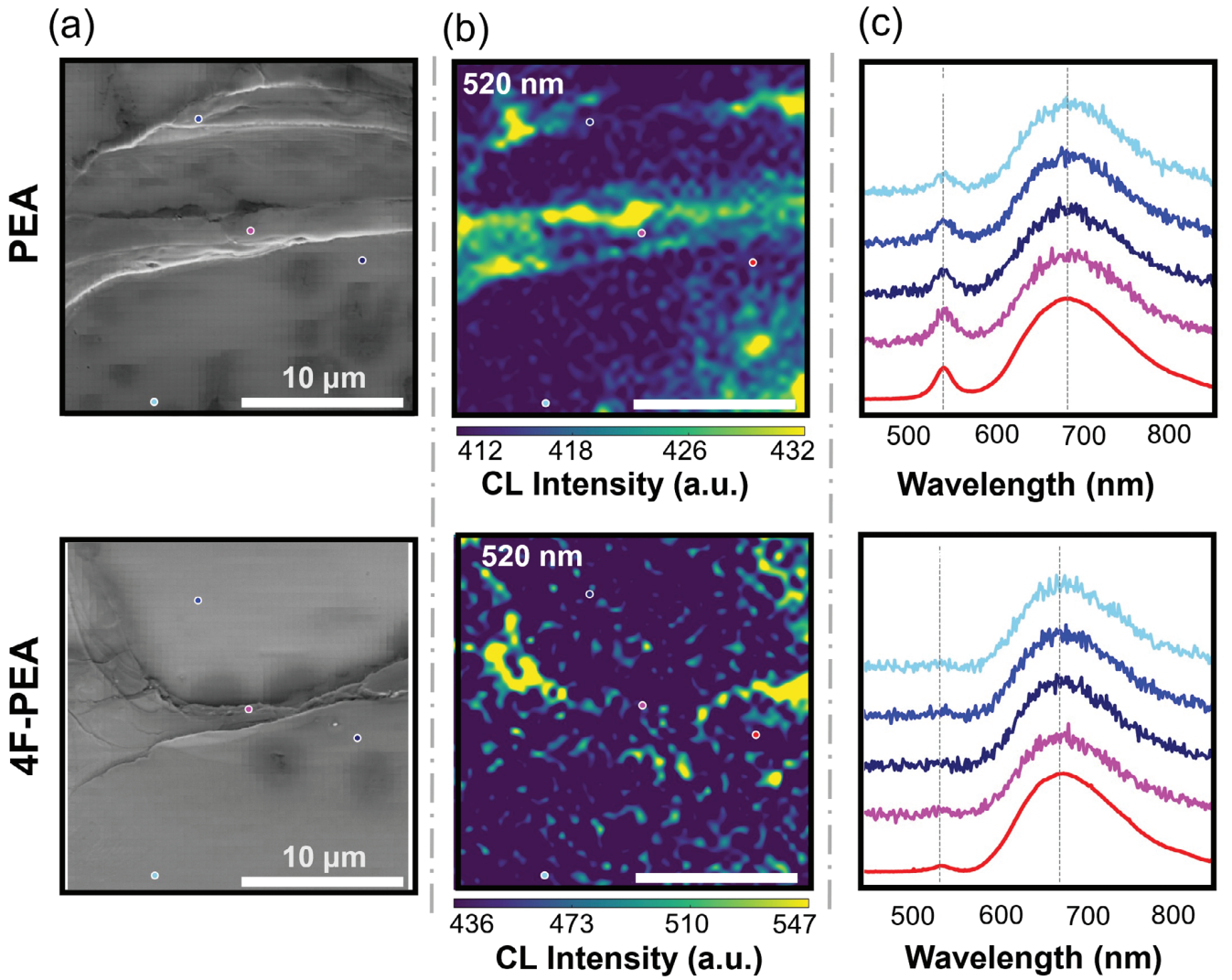

Figure 3. a) SEM images, b) 520 nm-filtered CL maps (assigned to segregated phase), c) local CL spectra of four spots color-marked on the maps of 2D Pb–Sn HP films with 90% Pb ratio, using PEA and 4F-PEA as spacer cations.

mixed Pb–Sn phases; the SEM image of the 4F-PEA sample reveals fewer boundaries between phases, which is attributed to the reduced phase segregation in this sample (Figure 3a). In particular, the broadband emission is uniformly distributed across the film, resulting in fewer distinct phase boundaries. The 690 nm-filtered CL maps of the films in Figure S6 (Supporting Information) also exhibit no specific spatial contrast in broadband emission which is attributed to the uniform distribution of the mixed phases across the films. The wavelengths of the segregated phase (520 nm) and the mixed Pb–Sn phase (690 nm) correspond to their respective CL peaks, as shown in the local CL spectra in Figure 3c. The lower intensity of the segregated phase in the 4F-PEA sample aligns with the PL results, further supporting our hypothesis for the reduced phase segregation in this film.

To further investigate the role of spacer engineering on phase segregation, time-resolved PL decays of the Pb–Sn films with 50% and 90% Pb content were measured using 1027 nm excitation wavelengths are shown in Figure S7 (Supporting Information). By employing a three-exponential peak fitting model, the average lifetime is calculated for each sample (Table S1, Supporting Information). Interestingly, for both Pb–Sn compositions, films containing 4F-PEA exhibit a longer carrier lifetime compared to those with PEA, while 4Cl-PEA shows the shortest average lifetime. This is likely attributed to the passivation of defects; stronger and more feasible coordination of 4F-PEA toward the inorganic lattice reduces non-radiative recombination centers. The lifetimes of the other systems exhibit notably shorter PL lifetimes notwithstanding small FWHM differences. This suggests that the spacer coordination action becomes weaker, thereby leaving larger amounts of defects in the 2D HP lattice.[30] Here, we hypothesize that, the larger size of the chlorine atom in 4Cl-PEA contributes to greater structural distortions, increasing phase segregation and reducing the overall stability of the material.[31,32]

To investigate the impact of halogen groups on PEA-based 2D Pb–Sn HP crystal structure, X-ray Diffraction (XRD) patterns were collected from the films containing three selected Pb–Sn

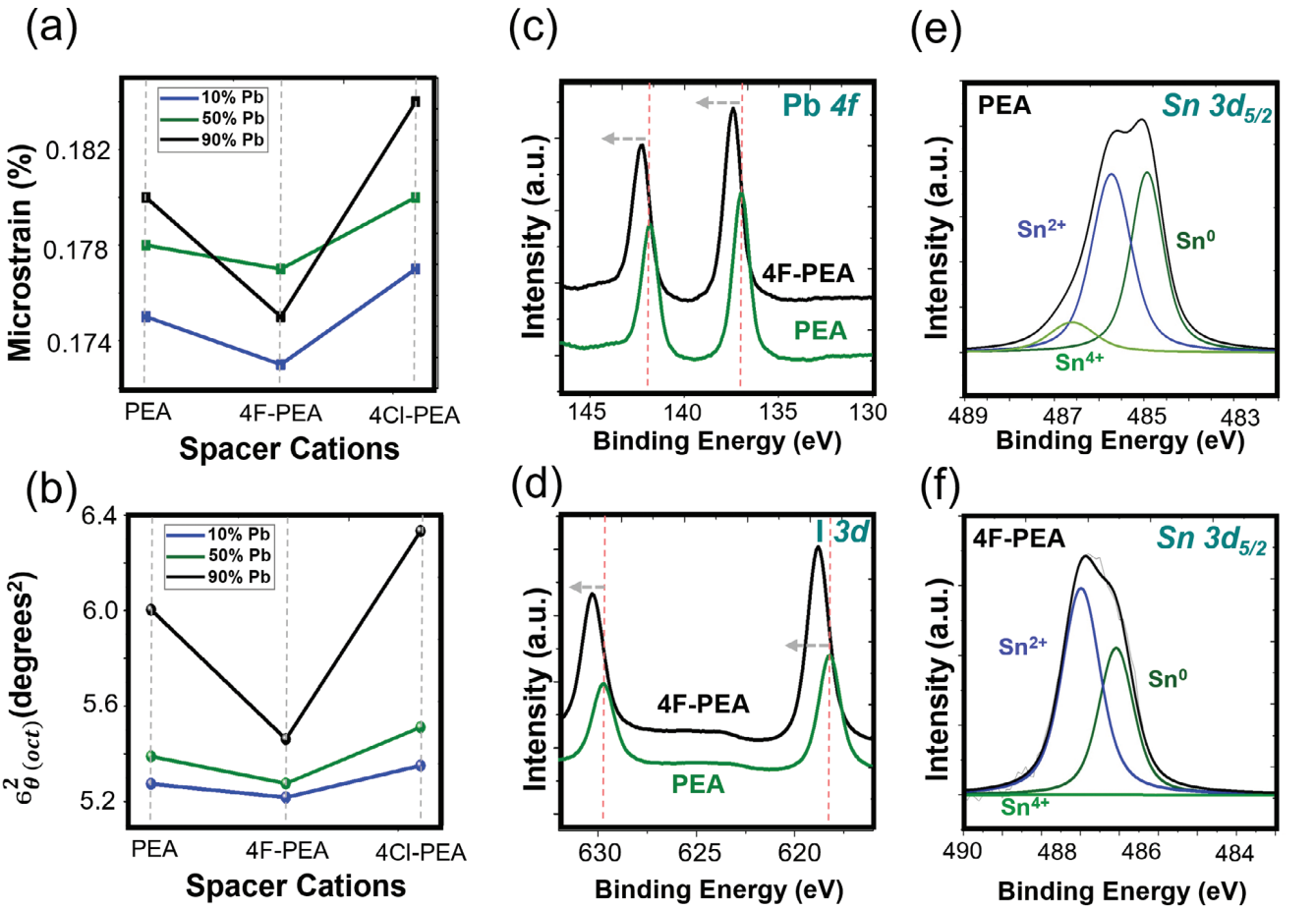

Figure 4. a) microstrain calculated from XRD refinement data and b) estimation of the degree of the distortion of the 2D Pb–Sn HP films with selected Pb ratios and three spacer cations. c) XPS spectra of Pb *4f* and d) I *3d*, e,f) Peak-deconvoluted Sn $3d_{5/2}$ spectra, of the 2D Pb–Sn HP films with 90% Pb and using PEA and 4F- PEA as spacer cations.

ratios and spacers. All films exhibit distinctive diffraction patterns of 2D HPs[33] which are displayed in Figure S8 (Supporting Information). For the composition containing 10% Pb, using 4Cl-PEA a significant degradation occurs, as indicated by the emergence of PEAI peaks (Figure S8a, Supporting Information). However, using 4F-PEA results in higher peak intensities across all Pb–Sn compositions, which is attributed to the enhanced crystallinity of the samples with this spacer cation. The peak shift to lower angles with the addition of F and Cl to the PEA corresponds to the increased distance between the inorganic planes, attributed to the larger sizes of the spacer cations by the substitution of *para*-H in phenyl ring with halogens, which shows a following order: 4Cl-PEA > 4F-PEA > PEA. More in detail, Rietveld refinement of the XRD-diffractograms (using the Double–Voigt approach based on Caglioti equation, Figure S9, Supporting Information)[34] assigns the crystalline structures of 2D HPs to the triclinic $P\bar{1}$ space group. The corresponding lattice cell parameters are listed in Tables S2 and S3 (Supporting Information). FWHM of the peaks is directly related to both the average size of the crystalline domains and the degree of distortion (microstrain) present in the crystalline lattice. A detailed size and strain analysis was conducted on the Pb–Sn HPs films (Note S1, Supporting Information), with the results shown in **Figure** 4a, highlighting significant differences in the microstructure of the three spacer cation samples. The analysis reveals that compositions with higher Pb content generally exhibit greater microstrain, regardless of the spacer cation used which is attributed to more defects and phase segregation in the samples.[18] Microstrain in the lattice can lead to distortions, which influence the overall stability of the crystalline structure. The reduced distortion observed in the 4F-PEA samples may be due to stronger interactions between the F cations and the inorganic layer as explained previously. These interactions likely enhance the rigidity of the inorganic lattice, resulting in a more stable and less defective system. On the other hand, the higher microstrain in 4Cl-PEA samples could suggest weaker interactions and more pronounced lattice distortions, contributing to a less stable crystal structure with more defects. In addition, Table S3 (Supporting Information) presents the lattice parameters, where it is observed that all lattice angles deviate from 90°, consistent with the triclinic structure of the samples.[35] Notably, the deviations in the samples containing 4F-PEA are smaller compared to the others, indicating a less distorted lattice. The degree of distortion of the perovskite octahedra can be characterized by the variance of the angles showing in Equation (1).[36] We estimated the degree of distortion, as shown in Figure 4b. The results indicate that

4F-PEA exhibits lower distortion, while 4Cl-PEA shows higher distortion in all Pb–Sn compositions.

$$\sigma^2_{\theta(\mathrm{oct})} = \frac{1}{11}\sum_{i=1}^{12}\left(\theta_i - 90^\circ\right)^2 \quad (1)$$

To assess the impact of fluorinated PEA as a spacer cation on defect states, X-ray photoelectron spectroscopy (XPS) measurements were performed on 2D Pb: Sn HP samples and Sn *3d*, Pb *4f*, and I *3d* spectra were extracted from that. Figure 4c shows Pb *4f* XPS spectra of the films with 90% Pb and using PEA and 4F-PEA as spacer cations. Two peaks are observed at ≈138 and ≈142 eV,[37] which are shifted to higher binding energies with the use of 4F-PEA. This shift indicates stronger interactions between Pb and its surrounding environment, as the higher dipole moment of F enhances the interaction between the F cation and the inorganic lead–halide framework. Specifically, the observed shift in the Pb *4f* XPS spectra to the lower binding energy in the samples containing fluorinated PEA spacer cations can be attributed to an increase in the electronic density around the Pb atoms compared to samples with PEA. However, this change is closely related to the nature of the interactions between the fluorine atoms and the inorganic layers within the perovskite lattice.[38] Fluorine, due to its high electronegativity, creates a polar interaction with the inorganic lead–halide framework.[39] While it tends to withdraw electron density from the surrounding lattice locally, its interaction with the Pb atoms redistributes electronic density in a way that stabilizes the entire system. This stabilization occurs because the strong bonding between fluorine and the inorganic octahedra minimizes structural distortions and defects, thereby creating a more cohesive lattice. The polar nature of the fluorinated spacer cation and its ability to form stronger electrostatic and hydrogen-bond-like interactions with the inorganic layer enhances the uniformity of the electron cloud surrounding Pb. These interactions effectively lower the overall energy of the Pb electronic states, leading to a decrease in the binding energy observed in the XPS spectra. This decrease reflects the more stable and defect-reduced environment facilitated by the fluorinated spacer cation. Thus, the electronic density changes around Pb are a direct consequence of the fluorinated spacer cation's interaction with the inorganic layers. Shifting to higher binding energies observed in I *3d* spectra with the use of 4F-PEA (Figure 4d), also suggesting stronger interaction similar to Pb *4f* spectra. Additionally, Sn $3d_{5/2}$ spectra are deconvoluted into three distinct components: metallic Sn (Sn^0), Sn^{2+}, and Sn^{4+}, centered at 484, 486, and 487 eV, respectively (Table S4, Supporting Information).[40] Figure 4e,f displays the Sn $3d_{5/2}$ spectra for films with 90% Pb. Interestingly, it is observed that using 4F-PEA suppresses the formation of Sn^{4+} and clearly reduces Sn^0, the product of Sn oxidation. Figures S10 and S11 (Supporting Information) present similar trends in the XPS spectra of samples containing 50% and 10% Pb, respectively. Despite a different sample composition, the suppression of Sn^{4+} formation and the reduction of metallic Sn are similarly evident with the use of 4F-PEA. Moreover, analogous shifts in the Pb *4f* and I *3d* spectra are noticeable with 4F-PEA, showing stronger interaction. These results demonstrate that 4F-PEA can effectively reduce Sn defects in 2D Pb–Sn HPs, leading to a longer carrier lifetime and reduced microstrain. This defect reduction also contributes to a decrease in the FWHM of the broad emission, as defects play a significant role in peak broadening.[12,18] By minimizing these defects, 4F-PEA improves the crystalline quality and optical properties of the material.

Finally, in **Figure 5**, we illustrate the mechanism by which adding halogen groups to PEA-based 2D Pb–Sn HPs influences structural distortion and therefore photophysical behavior.

3. Conclusion

This study provides a novel exploration into the use of halogen groups (F and Cl) in PEA-based 2D Pb–Sn HPs, emphasizing their significant impact on broadband PL emission. By systematically adjusting the Pb ratio and the type of spacer cations, we uncovered mechanisms that strongly influence phase segregation and emission behavior. Our findings show that using 4F-PEA improves both PL and structural properties, reducing emission FWHM and minimizing phase segregation, leading to more stable and efficient emission profiles. X-ray spectroscopy results (XRD and XPS) further confirm that the use of fluorinated PEA enhances crystallinity and reduces microstrain and defects, owing to fluorine's high dipole moment and stronger bonding with the inorganic octahedra. In contrast, chlorine's larger size induces lattice distortion and increases defects, negatively impacting the material's structural integrity. More importantly, this study exemplifies how the fundamental properties of chemically complex materials can be comprehensively explored in an accelerated manner through an unconventional high-throughput automated experimental workflow. Tuning broad emission is critical for achieving white light emission in LEDs. Moving forward, these findings could inform device fabrication by applying different halogen groups to examine their effects on emission properties, potentially enhancing the development of efficient white light sources.

4. Experimental Section

Materials: Phenethylammonium iodide (PEAI; Greatcell Solar Materials, 98%), 4-Flouro-Phenethylammonium iodide (4F-PEAI; Greatcell Solar Materials, 98%), 4-Chloro-Phenethylammonium iodide (4Cl-PEAI; Sigma-Aldrich, 98%), Tin(II) iodide (SnI_2; Sigma-Aldrich, 99.99%), lead (II) iodide (PbI_2; Fisher Scientific, 99.99% ultra-dry, metals basis), *N, N*-dimethylformamide (DMF; Sigma-Aldrich, 99.8% anhydrous), Dimethylsulfoxide (DMSO; Sigma-Aldrich, ≥99.9% anhydrous) were purchased and used without further purification.

High-Throughput Robotic Synthesis of 2D MHP Films: Stoichiometric quantities of X_2PbI_4 and X_2SnI_4 (0.3 M) (*X* = PEA, 4F-PEA, and 4Cl-PEA) were dissolved in a mixture solvent, DMF: DMSO (4:1 ratio), within an N_2-filled glovebox and stirred for five hours at room temperature. Subsequently, these solutions were transferred to a pipetting robot system maintained under an N_2 atmosphere. Fifty microliters of precursor solutions, representing 96 different Pb–Sn composition ratios, were dispensed into each well of a microplate. This was achieved using an Opentron OT-2 pipetting robot. For film depositions, the glass substrates were ultrasonically cleaned sequentially in deionized water, isopropanol, and acetone. After drying the substrates with nitrogen, they underwent a 55-minute UV ozone treatment. Immediately after the treatment, the substrates were transferred into a robot within an N_2 atmosphere and placed on a hotplate. The temperature of the hotplate was set to 100 °C. Precursor solution (0.5 µL each) was then dispersed onto the substrates using an 8-channel pipetting robot, a process that took only five minutes. After depositing all

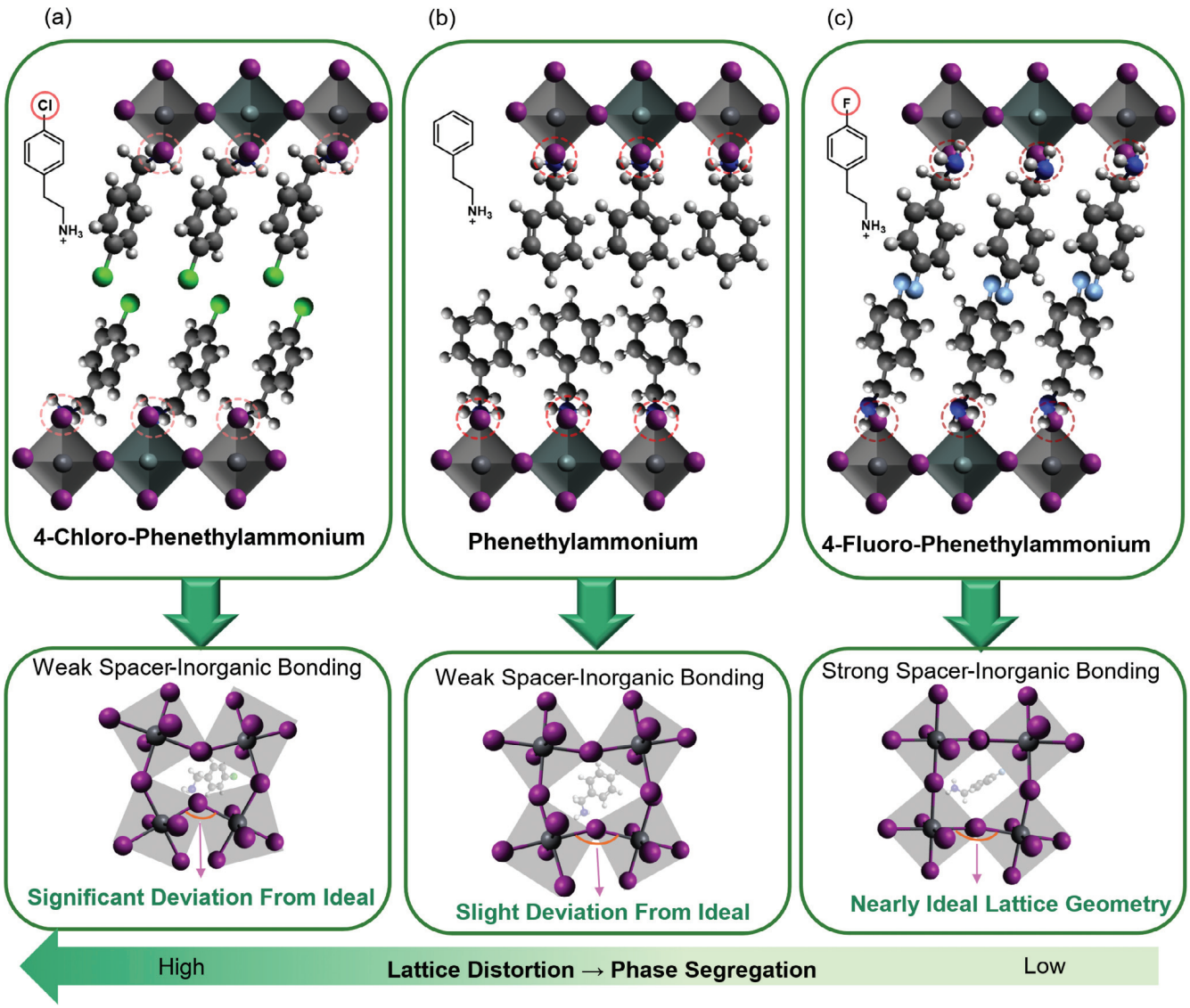

Figure 5. Structural representation of the effect of different spacer cations on lattice distortion in 2D Pb–Sn HPs. a) significant deviation from ideal lattice structure using Cl-PEA-based 2D HP, b) slight deviation in PEA, and c) nearly ideal lattice geometry in F-PEA-based HP.

96 compositions onto the substrates, they were left on the hotplate and annealed at 100 °C for 15 min, resulting in the formation of round films with 96 compositions.

This approach yielded three different data sets. The synthesis of these 288 different compositions (96 × 3) was completed in just three hours, with each set taking only 45 min. The high-throughput robotic system operated entirely within an N_2-filled enclosure, where both humidity and temperature were closely monitored and recorded for each experiment, before and during synthesis. For this specific experiment, the humidity was maintained at 0.5% RH at a temperature of 24 °C.

Photoluminescence Characterization: The drop-casted films were quickly transferred to the hybrid multi-mode optical reader (BioTek, Cytation 5), situated adjacent to the robotic system. PL spectra, with a 1 nm step resolution, were then collected from each well over time, using an excitation wavelength of 365 nm. A consistent "read" cycle was employed to gather 96 spectra from each film at 10-minute intervals, repeated across 100 cycles to obtain time-evolved PL spectra. This setup ensured that all films remained uninterrupted within the reader for the entire duration, thereby maintaining consistent time conditions for PL measurement across all compositions.

Data analysis was performed on Google Colab using Python. The code is available in the following link: (https://colab.research.google.com/drive/13I8453oPoY2fDMRANF80PnUNXzBRmMHx#scrollTo=ReQpBxOZrOVr).

Thin Film Fabrication: Stoichiometric quantities of X_2PbI_4 and X_2SnI_4 precursor solutions (X = PEA, 4F-PEA, and 4Cl-PEA) were dissolved in anhydrous DMF: DMSO mixed solvent with a 4:1 volume ratio. Thin films were subsequently cast on ITO substrates, which were first ultrasonically cleaned using deionized water, isopropanol, and acetone. After drying the substrates with nitrogen, they underwent a 20-minute UV ozone treatment and were immediately transferred to an N_2-filled glovebox for film deposition. The fabrication of these films included a two-step spin-coating process: initially 1000 rpm for 10 s, followed by 4000 rpm for 40 s. The films were annealed at 100 °C for 15 min.

Other Characterizations: XPS measurements were performed with a Scienta Omicron XPS Lab instrument using a monochromated Al Kα anode (1486 eV). Time Resolved PL decays were measured using a Horiba

Fluorolog 3 spectrometer and PPD-900 photon counting detector. XRD pattern of the films was acquired by using a high-resolution X-ray diffractometer (Malvern Panalytical, Empyrean). Hyperspectral Cathodoluminescence (CL) microscopy data were collected by using an environmental SEM instrument (FEI, Quattro) with a Delmic Sparc CL collection module. An e-beam with an acceleration voltage of 5 kV (beam current of 28 pA) with a dynamic acquisition time ranging 500–1000 ms was used for CL measurements. The pixel size was fixed to 500 × 500 nm^2. All measurements were conducted in a low vacuum environment of 0.27 Torr with H_2O vapor, which alleviated sample charging while minimizing electron-beam-induced damage.

Supporting Information

Supporting Information is available from the Wiley Online Library or from the author.

Acknowledgements

E.F. and M.A. acknowledge support from the National Science Foundation (NSF), Award Number 2043205, and Alfred P. Sloan Foundation, award No. FG-2022-18275. S.S. acknowledges partial support from the Center for Materials Processing (CMP) at the University of Tennessee, Knoxville. A.D. is grateful to German Academic Exchange Service (DeutscherAkademischer Austauschdienst: DAAD-PRIME 2023-24) postdoctoral researchers international mobility experience funding program. The XPS and CL experiments were supported by the Center for Nanophase Materials Sciences (CNMS), which is a US Department of Energy, Office of Science User Facility at Oak Ridge National Laboratory.

Conflict of Interest

The authors declare no conflict of interest.

Data Availability Statement

The data that support the findings of this study are available in the supplementary material of this article.

Keywords

2D Pb–Sn halide perovskites, defects, halogenation of spacer cation, high-throughput experiments, phase segregation

Received: November 14, 2024
Revised: December 16, 2024
Published online:

[1] J.-W. Lee, Z. Dai, T.-H. Han, C. Choi, S.-Y. Chang, S.-J. Lee, N. De Marco, H. Zhao, P. Sun, Y. Huang, *Nat. Commun.* **2018**, *9*, 3021.
[2] a) T. Zhou, H. Lai, T. Liu, D. Lu, X. Wan, X. Zhang, Y. Liu, Y. Chen, *Adv. Mater.* **2019**, *31*, 1901242; b) M. Shao, T. Bie, L. Yang, Y. Gao, X. Jin, F. He, N. Zheng, Y. Yu, X. Zhang, *Adv. Mater.* **2022**, *34*, 2107211; c) Z. Fang, X. Hou, Y. Zheng, Z. Yang, K. C. Chou, G. Shao, M. Shang, W. Yang, T. Wu, *Adv. Funct. Mater.* **2021**, *31*, 2102330.
[3] X. Lai, W. Li, X. Gu, H. Chen, Y. Zhang, G. Li, R. Zhang, D. Fan, F. He, N. Zheng, *Chem. Eng. J.* **2022**, *427*, 130949.
[4] a) F. Zhang, D. H. Kim, H. Lu, J.-S. Park, B. W. Larson, J. Hu, L. Gao, C. Xiao, O. G. Reid, X. Chen, *J. Am. Chem. Soc.* **2019**, *141*, 5972; b) J. Shi, Y. Gao, X. Gao, Y. Zhang, J. Zhang, X. Jing, M. Shao, *Adv. Mater.* **2019**, *31*, 1901673.
[5] Q. Li, Y. Dong, G. Lv, T. Liu, D. Lu, N. Zheng, X. Dong, Z. Xu, Z. Xie, Y. Liu, *ACS Energy Lett.* **2021**, *6*, 2072.
[6] A. Bala, V. Kumar, *ACS Appl. Energy Mater.* **2021**, *4*, 1860.
[7] a) Z. Wang, Q. Wei, X. Liu, L. Liu, X. Tang, J. Guo, S. Ren, G. Xing, D. Zhao, Y. Zheng, *Adv. Funct. Mater.* **2021**, *31*, 2008404; b) W. Fu, H. Liu, X. Shi, L. Zuo, X. Li, A. K. Y. Jen, *Adv. Funct. Mater.* **2019**, *29*, 1900221.
[8] J. Hu, I. W. Oswald, S. J. Stuard, M. M. Nahid, N. Zhou, O. F. Williams, Z. Guo, L. Yan, H. Hu, Z. Chen, *Nat. Commun.* **2019**, *10*, 1276.
[9] B. M. Lefler, S. J. May, A. T. Fafarman, *Phys. Rev. Mater.* **2020**, *4*, 120301.
[10] a) B. Zhao, M. Abdi-Jalebi, M. Tabachnyk, H. Glass, V. S. Kamboj, W. Nie, A. J. Pearson, Y. Puttisong, K. C. Gödel, H. E. Beere, *Adv. Mater.* **2017**, *29*, 1604744; b) C. C. Stoumpos, C. D. Malliakas, M. G. Kanatzidis, *Inorg. Chem.* **2013**, *52*, 9019; c) F. Faini, V. Larini, A. Scardina, G. Grancini, *MRS Bull.* **2024**, *49*, 1059.
[11] a) G. Xu, P. Bi, S. Wang, R. Xue, J. Zhang, H. Chen, W. Chen, X. Hao, Y. Li, Y. Li, *Adv. Funct. Mater.* **2018**, *28*, 1804427; b) X. Xu, C. C. Chueh, P. Jing, Z. Yang, X. Shi, T. Zhao, L. Y. Lin, A. K. Y. Jen, *Adv. Funct. Mater.* **2017**, *27*, 1701053.
[12] a) J. Yu, J. Kong, W. Hao, X. Guo, H. He, W. R. Leow, Z. Liu, P. Cai, G. Qian, S. Li, *Adv. Mater.* **2019**, *31*, 1806385; b) T. Li, X. Chen, X. Wang, H. Lu, Y. Yan, M. C. Beard, D. B. Mitzi, *ACS Energy Lett.* **2019**, *5*, 347; c) S. Kahmann, D. Meggiolaro, L. Gregori, E. K. Tekelenburg, M. Pitaro, S. D. Stranks, F. De Angelis, M. A. Loi, *ACS Energy Lett.* **2022**, *7*, 4232; d) C. Wang, Z. Song, C. Li, D. Zhao, Y. Yan, *Adv. Funct. Mater.* **2019**, *29*, 1808801; e) W. Qiu, Z. Xiao, K. Roh, N. K. Noel, A. Shapiro, P. Heremans, B. P. Rand, *Adv. Mater.* **2019**, *31*, 1806105.
[13] a) J. Luo, X. Wang, S. Li, J. Liu, Y. Guo, G. Niu, L. Yao, Y. Fu, L. Gao, Q. Dong, *Nature* **2018**, *563*, 541; b) S. Kahmann, E. K. Tekelenburg, H. Duim, M. E. Kamminga, M. A. Loi, *Nat. Commun.* **2020**, *11*, 2344; c) J. Yin, R. Naphade, L. Gutiérrez Arzaluz, J.-L. Bredas, O. M. Bakr, O. F. Mohammed, *ACS Energy Lett.* **2020**, *5*, 2149; d) D. Y. Park, S.-J. An, C. Lee, D. A. Nguyen, K.-N. Lee, M. S. Jeong, *J. Phys. Chem. Lett.* **2019**, *10*, 7942.
[14] a) J. Prakash, A. Singh, G. Sathiyan, R. Ranjan, A. Singh, A. Garg, R. K. Gupta, *Mater. Today Energy* **2018**, *9*, 440; b) N. J. Jeon, J. H. Noh, W. S. Yang, Y. C. Kim, S. Ryu, J. Seo, S. I. Seok, *Nature* **2015**, *517*, 476; c) K. A. Bush, K. Frohna, R. Prasanna, R. E. Beal, T. Leijtens, S. A. Swifter, M. D. McGehee, *ACS Energy Lett.* **2018**, *3*, 428; d) A. Hosseinmardi, A. Moshaii, S. Bazireh, K. Barakati, S. Abbasian, S. Karimi, M. Khodabandeh, *J. Nanopart. Res.* **2024**, *26*, 64.
[15] a) B. Li, B. Chang, L. Pan, Z. Li, L. Fu, Z. He, L. Yin, *ACS Energy Lett.* **2020**, *5*, 3752; b) L. Lanzetta, N. Aristidou, S. A. Haque, *J. Phys. Chem. Lett.* **2020**, *11*, 574; c) J. Xu, A. Maxwell, M. Wei, Z. Wang, B. Chen, T. Zhu, E. H. Sargent, *ACS Energy Lett.* **2021**, *6*, 4220.
[16] N. Aristidou, C. Eames, I. Sanchez-Molina, X. Bu, J. Kosco, M. S. Islam, S. A. Haque, *Nat. Commun.* **2017**, *8*, 15218.
[17] C. Li, Y. Pan, J. Hu, S. Qiu, C. Zhang, Y. Yang, S. Chen, X. Liu, C. J. Brabec, M. K. Nazeeruddin, *ACS Energy Lett.* **2020**, *5*, 1386.
[18] E. Foadian, J. Yang, S. B. Harris, Y. Tang, C. M. Rouleau, S. Joy, K. R. Graham, B. J. Lawrie, B. Hu, M. Ahmadi, *Adv. Funct. Mater.* **2024**, *34*, 2411164.
[19] a) Y. Zhao, J. Zhang, Z. Xu, S. Sun, S. Langner, N. T. P. Hartono, T. Heumueller, Y. Hou, J. Elia, N. Li, *Nat. Commun.* **2021**, *12*, 2191; b) S. L. Sanchez, Y. Tang, B. Hu, J. Yang, M. Ahmadi, *Matter* **2023**, *6*, 2900; c) Y. Wu, S. Lu, M.-G. Ju, Q. Zhou, J. Wang, *Nanoscale* **2021**, *13*, 12250.
[20] a) H. H. Fang, E. K. Tekelenburg, H. Xue, S. Kahmann, L. Chen, S. Adjokatse, G. Brocks, S. Tao, M. A. Loi, *Adv. Opt. Mater.* **2023**, *11*, 2202038; b) S. Narra, W.-C. Chen, A. Seetharaman, I.-H. Tsai, E. W.-G. Diau, *J. Phys. Chem. C* **2024**, *128*, 1207.

[21] I. García-Benito, C. Quarti, V. I. Queloz, Y. J. Hofstetter, D. Becker-Koch, P. Caprioglio, D. Neher, S. Orlandi, M. Cavazzini, G. Pozzi, *Front. Chem.* **2020**, *7*, 946.
[22] L. Zhang, Y. Jiang, Y. Feng, M. Cui, S. Li, X. Fu, H. Y. Hsu, C. Qin, M. Yuan, *Angew. Chem.* **2023**, *135*, 202302184.
[23] a) Y. Liu, W. Yan, S. Han, H. Zhu, Y. Tu, L. Guan, X. Tan, *Sol. RRL* **2022**, *6*, 2101100; b) R. Jacobs, J. Liu, H. Abernathy, D. Morgan, *Adv. Energy Mater.* **2024**, *14*, 2303684; c) Y. Lu, D. Wei, W. Liu, J. Meng, X. Huo, Y. Zhang, Z. Liang, B. Qiao, S. Zhao, D. Song, *J. Energy Chem.* **2023**, *77*, 200.
[24] X. Li, Y. Dan, R. Dong, Z. Cao, C. Niu, Y. Song, S. Li, J. Hu, *Appl. Sci.* **2019**, *9*, 5510.
[25] a) Q. Zhou, Q. Xiong, Z. Zhang, J. Hu, F. Lin, L. Liang, T. Wu, X. Wang, J. Wu, B. Zhang, *Sol. RRL* **2020**, *4*, 2000107; b) H. Xu, Y. Sun, H. Zheng, G. Liu, X. Xu, S. Xu, L. Zhang, X. Chen, X. Pan, *J. Mater. Chem. C* **2019**, *7*, 15276.
[26] a) F. El-Mellouhi, S. N. Rashkeev, A. Marzouk, L. Kabalan, A. Belaidi, B. Merzougui, N. Tabet, F. H. Alharbi, *J. Mater. Chem. C* **2019**, *7*, 5299; b) B. Luo, Y. Guo, Y. Xiao, X. Lian, T. Tan, D. Liang, X. Li, X. Huang, *J. Phys. Chem. Lett.* **2019**, *10*, 5271.
[27] a) Q. Cheng, B. Wang, G. Huang, Y. Li, X. Li, J. Chen, S. Yue, K. Li, H. Zhang, Y. Zhang, *Angew. Chem., Int. Ed.* **2022**, *61*, 202208264; b) S. Song, S. J. Yang, W. Choi, H. Lee, W. Sung, C. Park, K. Cho, *Adv. Energy Mater.* **2020**, *10*, 2001759.
[28] C. Qin, F. Zhang, L. Qin, X. Liu, H. Ji, L. Li, Y. Hu, Z. Lou, Y. Hou, F. Teng, *Adv. Electron. Mater.* **2021**, *7*, 2100384.
[29] a) J. Yang, D. K. LaFollette, B. J. Lawrie, A. V. Ievlev, Y. Liu, K. P. Kelley, S. V. Kalinin, J. P. Correa-Baena, M. Ahmadi, *Adv. Energy Mater.* **2023**, *13*, 2202880; b) H. Guthrey, J. Moseley, *Adv. Energy Mater.* **2020**, *10*, 1903840.
[30] a) P. K. Nayak, D. Ghosh, *J. Mater. Chem. C* **2023**, *11*, 3521; b) T. Zhou, Q. Li, L. Zhou, *Adv. Energy Mater.* **2024**, *14*, 2400050.
[31] L. Cheng, K. Meng, Z. Qiao, Y. Zhai, R. Yu, L. Pan, B. Chen, M. Xiao, G. Chen, *Adv. Mater.* **2022**, *34*, 2106380.
[32] N. Zhou, B. Huang, M. Sun, Y. Zhang, L. Li, Y. Lun, X. Wang, J. Hong, Q. Chen, H. Zhou, *Adv. Energy Mater.* **2020**, *10*, 1901566.
[33] J. Zhang, X. Zhu, M. Wang, B. Hu, *Nat. Commun.* **2020**, *11*, 2618.
[34] a) A. Dubey, *Universität Duisburg-Essen* **2023**, 2023; b) H. M. Rietveld, *Appl. Crystallogr.* **1969**, *2*, 65; c) G. Caglioti, A. Paoletti, F. Ricci, *Nucl. Instrum.* **1958**, *3*, 223.
[35] S. K. Radha, C. Bhandari, W. R. Lambrecht, *Phys. Rev. Mater.* **2018**, *2*, 063605.
[36] a) K. Robinson, G. Gibbs, P. Ribbe, *Science* **1971**, *172*, 567; b) E. Rönnebro, D. Noréus, K. Kadir, A. Reiser, B. Bogdanovic, *J. Alloys Compd.* **2000**, *299*, 101.
[37] M. Wei, K. Xiao, G. Walters, R. Lin, Y. Zhao, M. I. Saidaminov, P. Todorović, A. Johnston, Z. Huang, H. Chen, *Adv. Mater.* **2020**, *32*, 1907058.
[38] C. Li, N. Zhang, P. Gao, *Mater. Chem. Front.* **2023**, *7*, 3797.
[39] Y. He, Z. Chen, X. Chen, X.-M. Zhang, D. Fu, *Mater. Chem. Front.* **2022**, *6*, 1292.
[40] A. Wieczorek, H. Lai, J. Pious, F. Fu, S. Siol, *Adv. Mater. Interfaces* **2023**, *10*, 2201828.